Jupiter's Great Red Spot threatened by interactions with incoming anticyclones

A. Sánchez-Lavega[1], A. Anguiano-Arteaga[1], P. Iñurrigarro[1], E. Garcia-Melendo[2], J. Legarreta[1], R. Hueso[1], J. F. Sanz-Requena[3-4], S. Pérez-Hoyos[1], I. Mendikoa[6], M. Soria[2], J. F. Rojas[1], M. Andrés-Carcasona[2], A. Prat-Gasull[2], I. Ordoñez-Extebarria[1], J.H. Rogers[6], C. Foster[7], S. Mizumoto[8], A. Casely[9], C.J. Hansen[10], G.S. Orton[11], T. Momary[11] and G. Eichstädt[12]

[1]Escuela de Ingeniería de Bilbao, Universidad del País Vasco UPV/EHU, Bilbao, Spain

[2]Universitat Politècnica de Catalunya UPC, Terrasa, Spain

[3] Universidad Europea Miguel de Cervantes, Valladolid, Spain

[4] Dpto. Física Teórica, Atómica y Óptica, Universidad de Valladolid, Valladolid, Spain

[5] Tecnalia Research and Innovation, Bilbao, Spain

[6] British Astronomical Association, London, UK

[7] Astronomical Society of Southern Africa, Centurion, South Africa

[8] Association of Lunar and Planetary Observers ALPO-Japan, Chofu-city Tokyo, Japan

[9] Independent scholar, Sydney, Australia

[10] Planetary Science Institute, Tucson, AZ, USA

[11] Jet Propulsion Laboratory, California Institute of Technology, Pasadena, CA, USA

[12] Independent scholar, Stuttgart, Germany

Corresponding author: Agustín Sánchez-Lavega (agustin.sanchez@ehu.eus)

Key Points:

- In 2018-20 Jupiter's Great Red Spot interacted with series of anticyclones loosing part of its visible red area and distorted its shape.
- The GRS increased its tangential velocity, not changing its vorticity, but changing its 90-day oscillation in longitude.
- Dynamical and radiative transfer modeling show that the interactions affected the upper cloud of the GRS with no risk for its survival.

Abstract

Jupiter's Great Red Spot (GRS), a giant anticyclone, is the largest and longest-lived of all the vortices observed in planetary atmospheres. During its history, the GRS has shrunk to half its size since 1879, and encountered many smaller anticyclones and other dynamical features that might tend to erode it. In 2018-2020, while having a historically small size, its structure and even its survival appeared to be threatened when a series of anticyclones moving in from the east tore off large fragments of the red area and distorted its shape. In this work we report observations of the dynamics of these interactions and show that as a result the GRS increased its internal rotation velocity, maintaining its vorticity but decreasing its visible area, and suffering a transient change in its otherwise steady 90-day oscillation in longitude. From a radiative transfer analysis and numerical simulations of the dynamics we show that the interactions affected the upper cloud tops of the GRS. We argue that the intense vorticity of the GRS, together with its larger size and depth compared to the interacting vortices, guarantees its long lifetime.

Plain Language Summary

Jupiter's Great Red Spot (GRS) is a giant anticyclone with a length that has shrunk since 1879 from ~ 40,000 km to its current value of 15,000 km. The GRS is the longest-lived of all the planetary vortices, observed perhaps since the 17th century. During its history, the GRS has encountered a variety of smaller anticyclones and other dynamical features, surviving to these interactions. In 2018-2020, series of anticyclones interacted with it, tore off large fragments of its red area (called "flakes"), eroding and distorting its oval shape, and apparently threatening its survival. The interactions produced an increase in the GRS internal rotation velocity accompanied by a transient increase the period and amplitude of its steady 90-day oscillation in longitude. From the analysis of the reflectivity of the GRS and flakes and model simulations of the dynamics of the interactions we find that these events are likely to have been superficial, not affecting the full depth of the GRS. The interactions are not necessarily destructive but can transfer energy to the GRS, maintain it in a steady state, guaranteeing its long lifetime.

1 Introduction

Jupiter's Great Red Spot is the archetype and the best studied of all the vortices in the giant planets, but its origin and fate remain mysterious. The first detailed studies of this anticyclone started with the Voyager 1 and 2 flybys in 1979 when its velocity field, vorticity and temperature structure at the upper cloud level were measured (Mitchell et al., 1981; Flasar et al., 1981; Conrath et al., 1981). Over the past 130 years, the GRS has decreased in size by half (Simon et al., 2018; Rogers, 1995) and has undergone numerous interactions with a variety of different dynamical features (anticyclonic vortices and open circulating cells called South Tropical Disturbances, STrD) that develop at its latitude east and west of its location (Rogers, 1995; Smith et al., 1979; Sánchez-Lavega et al., 1998, 2013; Li et al., 2004; Sada et al., 1996). Throughout 2018-2020 a series of interactions took place between the GRS and anticyclonic vortices (AV) coming from the east, as observed in previous cases (Smith et al., 1979; Sánchez-Lavega et al., 1998; Li et al., 2004). The new events here studied were particularly interesting for three reasons.

First, the GRS at the time had the smallest size in its history. Second, the vortices had a medium size, ~ 2.5-5% of the GRS area, and were numerous, such that they collided with the GRS one after another. Third, the encounters gave rise to strong interactions of a type rarely recorded before. All this significantly disrupted the red oval area of the GRS, and was even suspected of putting its long life at risk.

2 Materials and Methods

An alert was circulated by the amateur community early in 2019 on the GRS's events (nicknamed as "flakes") and a large number of images were gathered during that year by observers contributing to open planetary image repositories (Table S1) (Foster et al., 2020). Additional images in the visual and near-infrared spectral ranges were obtained from 27 to 30 May 2019 with the 2.2-m telescope at Calar Alto Observatory using the instrument PlanetCam (Mendikoa et al., 2016) that were photometrically calibrated (Mendikoa et al., 2017) and used for a radiative transfer analysis. We also used observations obtained in 2018-2020 with JunoCam on the Juno spacecraft ant the Hubble Space Telescope (HST) (Table S2). We focus in this study on the epochs when most active interaction episodes occurred from May to July 2019 (Table S2).

2.1 Measurement of ground-based images

We used the software WinJupos to navigate Jupiter's images from telescope observations, map project them and measure the features position (WinJupos, 2020). The motions of the features were measured in two ways: (1) when the displacements are short in time and the trajectory can be considered a straight line in longitude or latitude, we used series of images to track the motion (a minimum is always an image pair), limited by the spatial resolution and time interval, then making a linear fit to retrieve their mean drift rate (degrees/day) in latitude and longitude, and converting displacements in zonal and meridional velocities; (2) when the trajectory is curved, we integrate the motion along a curved path represented by the arc of an ellipse following the GRS flow and adjusting the center of the ellipse. In most cases this trajectory is well represented by the arc of an ellipse in correspondence with the GRS flow. We then superimposed an ellipse to the points representing the trajectory of the feature in the longitude-latitude map and manually fit the track with a pointer to adjust the center of the ellipse and determine its minor and major axis. We then calculate the length of the arc of the ellipse traced by the motion of the feature and retrieve the average velocity after dividing by the time interval between the first and last dates that determine the trajectory. Errors in wind measurements retrieved from features tracking in ground-based images were estimated as the image resolution divided by the tracking time ~ 400 – 600 km/(20 hrs) ~ 5-10 ms^{-1}.

2.2 Measurement of HST images

The original images were navigated and projected into cylindrical maps using the WinJUPOS software (WinJupos, 2020). Maps were corrected from limb darkening effects using a Lambert law and the contrast of features was enhanced using high-pass image filters. Then we used the PICV (Particle Image Correlation Velocimetry) image correlation software (Hueso et al., 2009) to

track the motions of cloud features from measurements of the displacement of features in pair of HST images separated by 1.59 h. The software examined correlation of image windows of 1°-3° depending on the features location in different areas of the images. Most of the measurements were made with boxes of 1°x1° or 1.2°x1.2°. All measurements (3,253 individual wind vectors in Fig. 1) were validated by a human operator who visually checked each individual identification and correlation map produced by the software. To compute a continuous velocity field we interpolated the wind vectors into a regular grid of 0.1° and smoothed to a resolution of 1°. This wind field was used to compute the mean zonal and meridional profiles along the centre of the GRS (Fig. 1) and the vorticity field (Fig. 2).

2.3 Mapping JunoCam images

The raw JunoCam images were taken from the Reduced Data Record (RDR) product and have been corrected from the instrumental effects and adjusted the scaled levels of radiance (Caplinger et al., 2016). The image processing, map projection and navigation of the images was carried out using the ISIS software (Integrated Software for Imagers and Spectrometers) using the Juno trajectories available in SPICE kernels (Acton et al., 2016). After projecting each sector that makes up the image, we grouped all of them into a final map using the GDAL libraries (GDAL/OGR, 2020). Finally we combine the different filtered Red, Green and Blue images to the resulting color RGB image. Further details on the navigation of details of JunoCam images and maps of the GRS are given in (Sánchez-Lavega et al., 2018 and references therein).

2.4 Radiative transfer analysis

Data obtained from PlanetCam-UPV/EHU for the two regions of interest at two similar geometrical configurations were photometrically calibrated in absolute reflectivity using calibration standard stars (SP1741+054 or Kopff-27 and HD84937 for the visible; HD102870 for visible and SWIR wavelengths) (Mendikoa et al., 2017). The spectral dependence of reflectivity was modeled with the NEMESIS code (Irwin et al., 2008), which uses the optimal estimator scheme to retrieve the most likely atmospheric parameters that best fit the observed reflectivity. We assume Jupiter's atmosphere to be a mixture of H2 and He, which produce Rayleigh scattering (Taylor et al., 2004), and CH4, whose absorption was added as pre-computed correlated-k tables from previous absorption coefficients (Karkoschka et al., 2010). Further details are given in section 3.3.

3 Results

Figure 1 puts in context the GRS cloud morphology and dynamics in April 2018, one year before the period of the strongest interactions, from images taken with JunoCam on the Juno spacecraft and the Hubble Space Telescope (HST). At this time a large STrD was streaming past the GRS (Rogers et al., 2018) so thin streamers of red clouds can be seen at the eastern and western sides of the red oval (Figures 1a, 3). Nevertheless, the GRS velocity and vorticity maps (Figure 2) were similar to those reported for the 2012-2017 period (Simon et al., 2018; Sánchez-Lavega et al., 2018). The GRS showed a maximum averaged velocity $u_{NS} \sim 120$ ms^{-1} at the north and south edges

of the red oval whereas the meridional peak velocities were smaller and different at the western ($v_W \sim 70$ ms^{-1}) and eastern ($v_E \sim 110$ ms^{-1}) sides (Figure 1d). The GRS flow had a ring of maximum vorticity with peak value $\zeta_V = 6\text{x}10^{-5}$ s^{-1}, as reported in previous studies (Mitchell et al., 1981; Simon et al., 2018) (Figure 2).

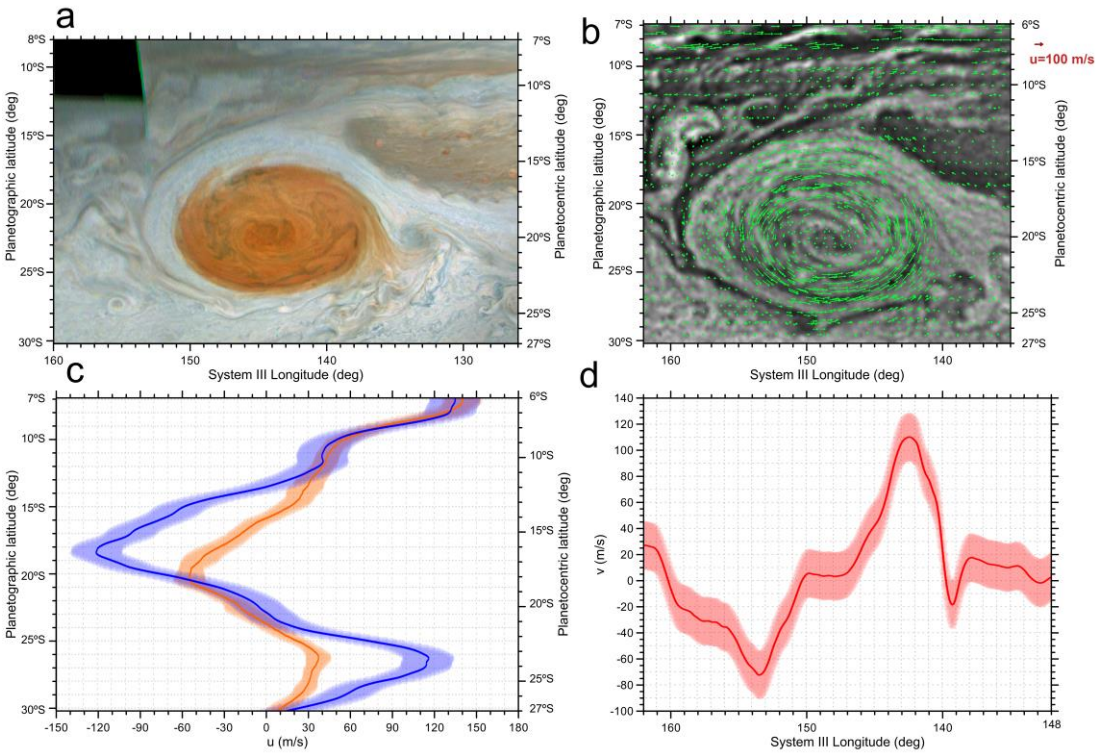

Figure 1. *The GRS cloud morphology and wind field in 2018. (a) Juno/JunoCam mapped image obtained in perijove PJ12 on 1 April 2018; (b) HST/WFC3 image obtained on 17 April 2018 (OPAL program, Wong et al., 2020) in filter 631 nm with superimposed measured wind vectors; (c) Averaged zonal wind profile along the North-South major axis of the GRS (blue line with velocity uncertainty shadowed) compared to the mean zonal velocity profile (orange line); (d) Averaged wind profile along the east-west major axis of the GRS. The GRS red oval is centered at planetographic latitude 22.6°S ± 0.4° and shows in its interior similar features to those described in detail a year before (Figure 1a) (Sánchez-Lavega et al., 2018). Surrounding there is a white ring (wider in the northern part, a region historically called the "hollow"). The GRS anticyclonic flow encompasses both regions (red oval and hollow) as it can be seen from the wind field measurements (Figure 1b). A comparison with the ambient winds shows the correlation with the jet peaks and dynamical extent of the GRS (Figure 1c). In the north edge of the hollow, there is a discontinuity or gap at approximate latitude 10°S and longitude 141°III (Fig. 1a), an opening in the circulation that allows the fluid elements to escape from the hollow in the northeast direction where they are carried eastward by the ambient zonal flow (Sánchez-Lavega et al., 1998). This gap is limited to the east by a stagnation region of low albedo clouds (latitude 13°S, 138° III, Fig. 1a) (Sánchez-Lavega et al., 2018). The gap and stagnation regions form and disappear over time*

and affect the AV interaction with the GRS. Planetographic latitudes and System III West longitudes are used throughout this article.

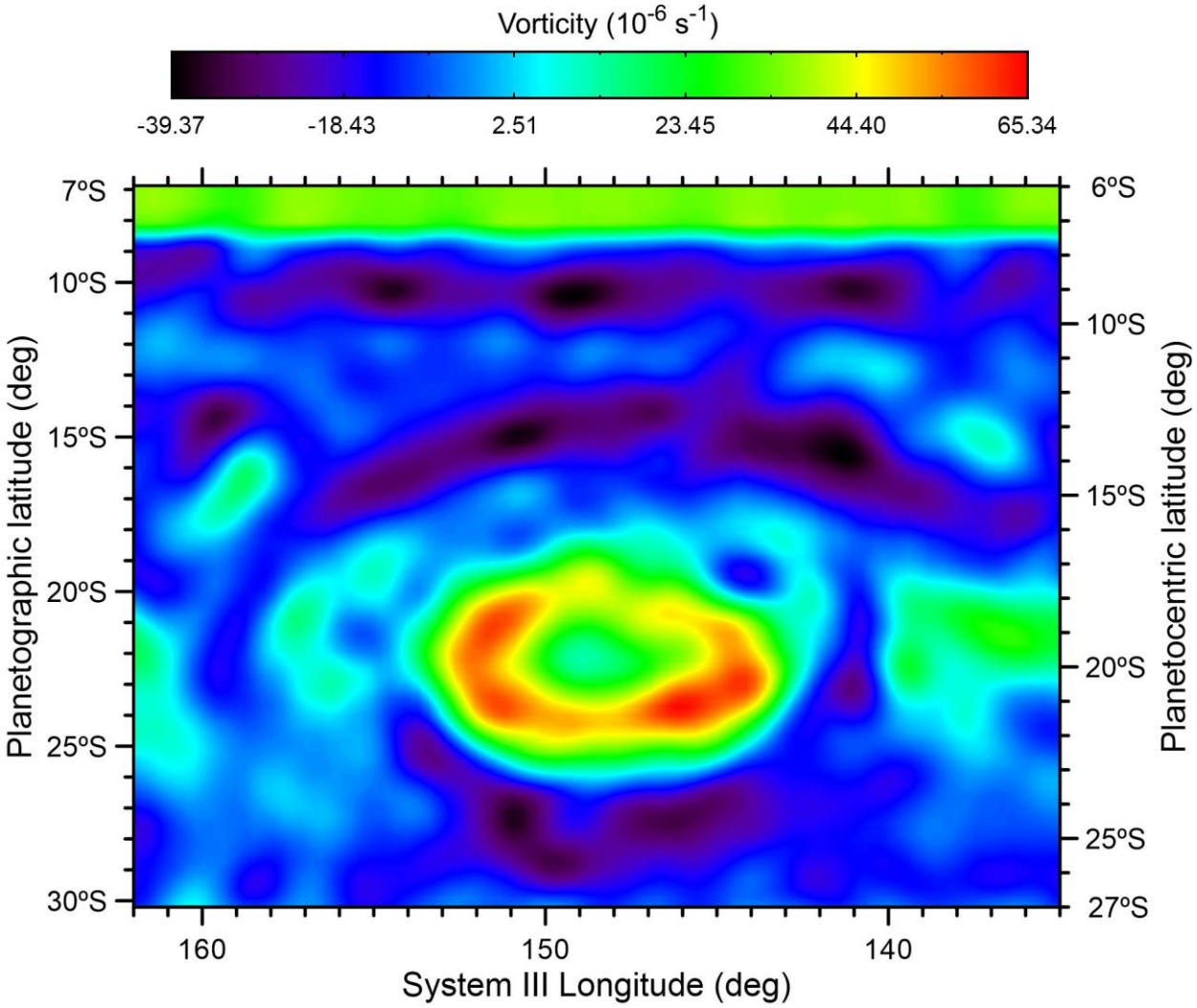

Figure 2. *Vorticity map of the GRS. Values of the vorticity obtained from the velocity measurements presented in Figure 1b. The methodology followed to calculate the vorticity and its precision is explained in detail in Hueso et al. (2009).*

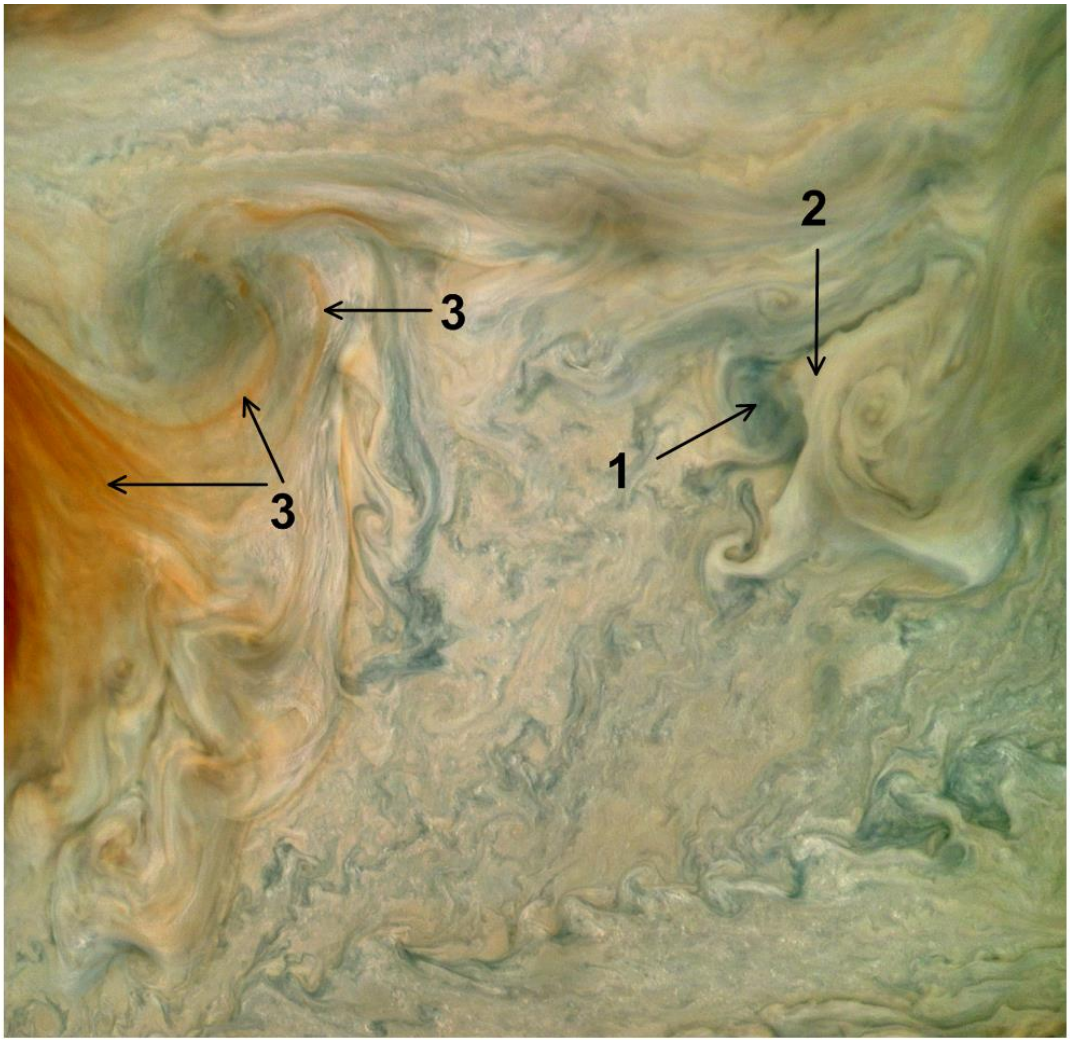

Figure 3. *East side of the GRS observed by JunoCam on 1 April 2018. This enlarged map from Figure 1a shows aerosol layers at different altitudes. At least three can be distinguished: (1) Deep low albedo cloud; (2) white intermediate haze/cloud; (3) high red chromophore haze. Comparing with the radiative transfer model, 1 and 2 could correspond to the upper cloud deck and 3 to the tropospheric haze.*

3.1 Phenomenology of the interactions

The anticyclonic vortices (AV) that interacted with the GRS appeared as white ovals surrounded by a low-albedo ring (Figure 4). The AVs were centered at planetographic latitude ~ 20°S-21°S, had a characteristic size of ~ 5,000 km (east-west) by 3,500 km (North-South) and moved westward (towards the GRS) at an absolute speed of ~ 40 ms^{-1}, in agreement with the ambient wind profile (Figure 1c). When reaching the eastward edge of the GRS they are entrained by its anticyclonic flow, moving inside the northern collar (Figure 4a). Because the width of the hollow is similar to the size of AVs, they were compressed, stretched and fragmented (Figure 4 b-d), then skimming the outer edge of the red oval, they tore off material producing the streamers and

flakes of red material that moved outward from the red oval (Figure 4e-f). In some cases, the remnants from the AVs along with the material that had been ripped off fully circumnavigated the red oval, moving along the southern edge of the GRS and detaching from it at its east edge at latitude 25°S - 26°S. In other cases they were expelled out of the GRS at its west edge. Additional examples of such interactions are shown in Figure 5. Descriptions, images and details of a large number of these events are given by Foster et al. (2020). Encounters of similar AVs with the GRS were observed in image sequences from the Voyager 1 flyby in 1979 (Smith et al., 1979; Rogers, 1995; Sada et al., 1996). At that time the GRS was large and exhibited complex cloud morphology, and apparently was less disrupted by the interactions, although some AV material was eventually pulled into the GRS.

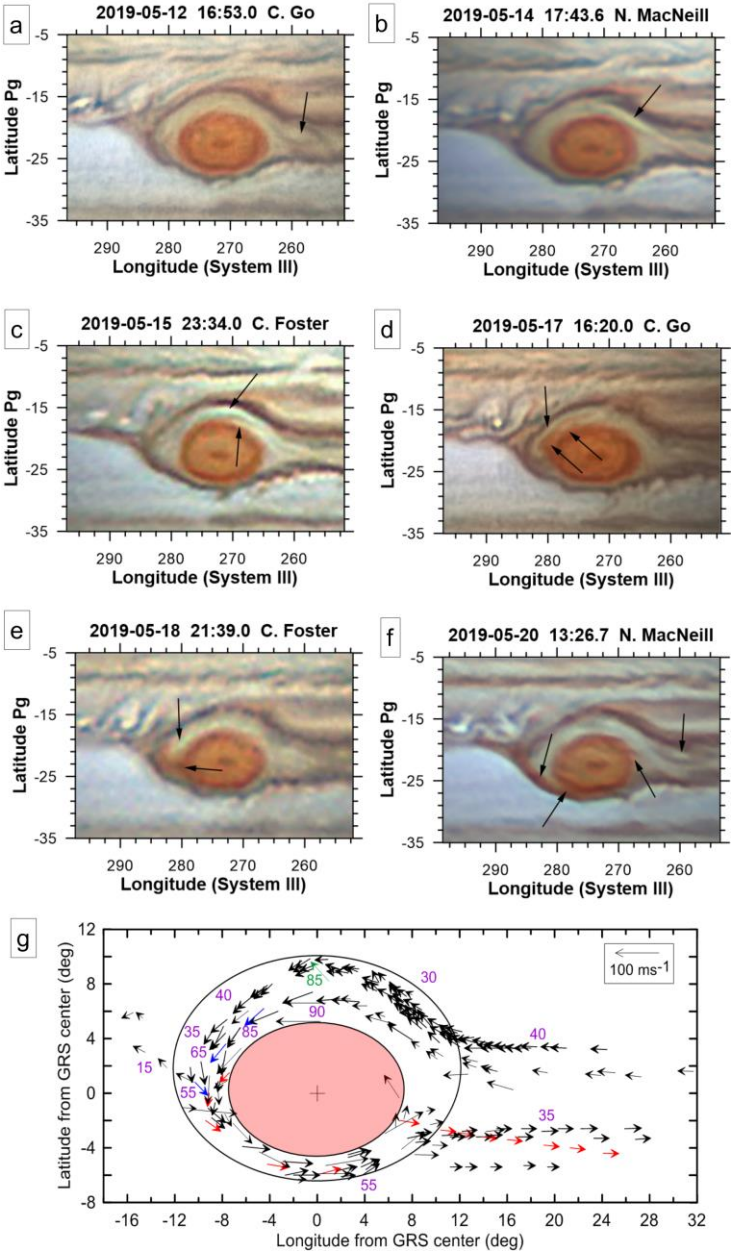

Figure 4. *Interactions of anticyclones with the GRS. (a-f) This sequence of mapped colour composite RGB images shows the full interaction of one AV with the GRS from 10 to 20 May 2019. Dates, times and observers are identified in each panel. Arrows mark the location of the AV and its fragments and the flake formation on the west side of the GRS. Note that a new AV is entering the collar in (f). Other sequences of interactions are presented in Foster et al. (2020). (g) Wind vectors derived from cloud tracking from May 10 to June 10, 2019. The ellipses represent the red oval (red area) and outer periphery ring (open in the east edge).The red and blue vectors correspond to strong AV interactions and flake formation. Numbers (purple) give the value of the velocity in ms^{-1}. The green vector shows a particular velocity measured for an AV moving rapidly to the gap region on 16 April 2020.*

Figure 4g shows the wind measurements between 11 and 29 May 2019 outside the red oval (i.e. along the GRS periphery and hollow) as derived from tracking the AV features, their fragments, and the streamers and flakes ripped from the red oval. Representative values of the drift velocity (in ms^{-1}) in the different sectors are given in the figure with velocity errors estimates ~ 5-10 ms^{-1} (section 2.1). During this period the gap in the outer edge of the hollow at it northernmost point was closed, favoring the interactions by closing the alternative path of flow of the AVs out of the GRS hollow. Features interacting with the red oval edge moved at speeds up to 90 ms^{-1}. Upon interaction, the features slowed down rapidly in a short distance or even diluted and merged with clouds in the GRS collar disappearing. We have measured decelerations of an AV fragment forming a flake from 93 ms^{-1} to 19 ms^{-1} followed by the recovering of its speed to 90 ms^{-1} (Figure 4d-f). As a consequence of these interactions the red oval showed important distortions from its elliptical shape (Figures 4d, 5). Detailed views of the GRS and its streamers and flakes in 2018-2019 can be seen in the high-resolution images occasionally obtained by JunoCam on board Juno (Figure 6).

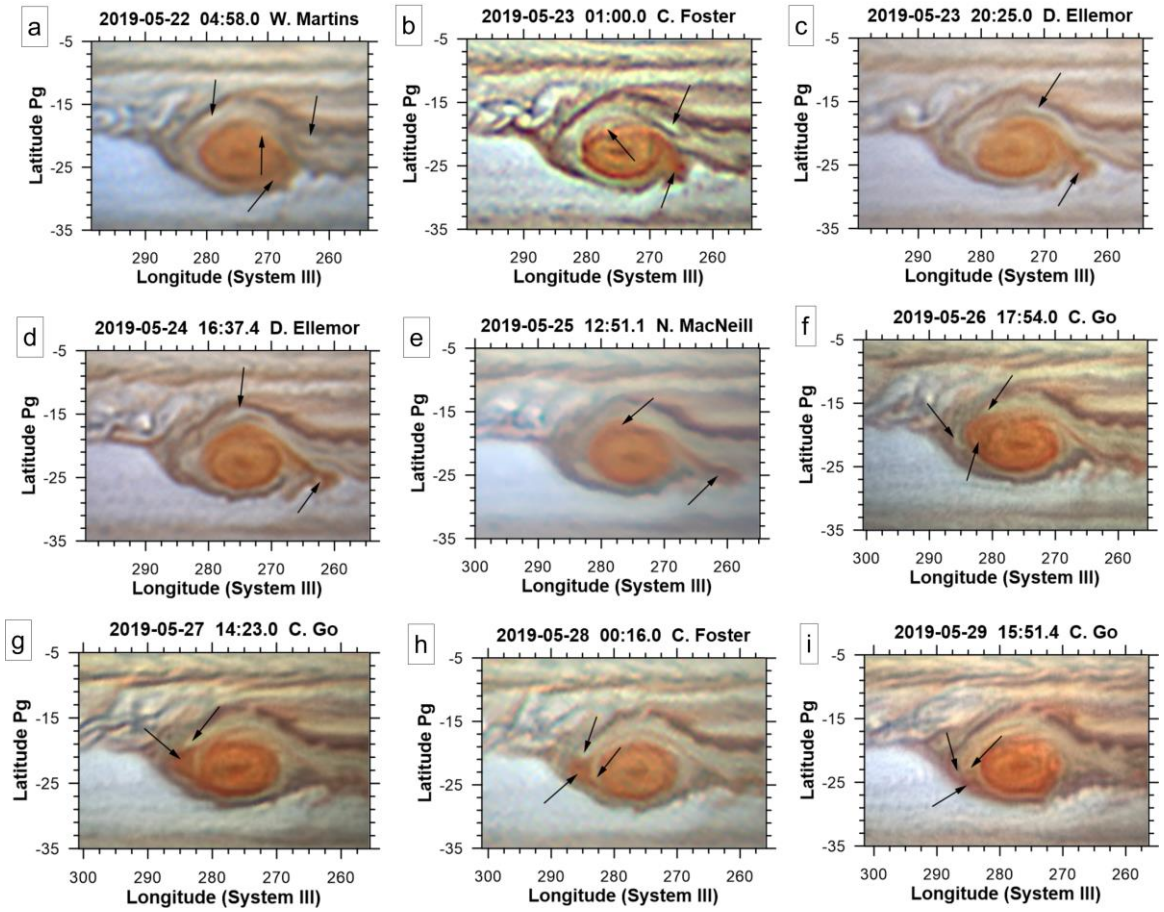

Figure 5. *Anticyclones AV interacting with the GRS. A sequence of mapped colour composite RGB images showing the interaction of an AV anticyclone with the GRS from May 22 to 29, 2019. The date and observers are identified in each panel. The arrows mark the location of the AV and its fragments, the flake formation in the East side of the GRS, and a white cloud impinging on the GRS red oval.*

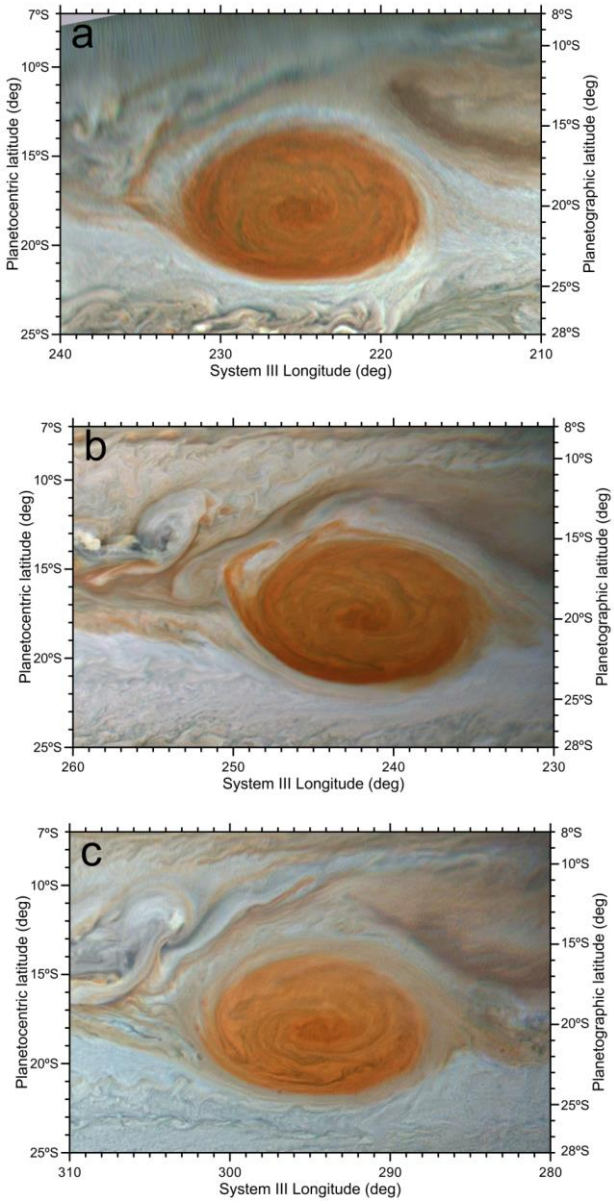

Figure 6. *The GRS observed at high resolution by JunoCam. The maps correspond to the following dates: (a) Perijove 17 (21 December 2018). A large streamer at the west edge with a width ~1,250 km is flowing away from the red area toward the hollow outer edge. The gap is open and the stagnation region well defined. (b) Perijove 18 (12 February 2019). A flake has formed with white clouds between it and the red oval. A ring of reddish material surrounds the east side of the red oval, probably due to a previous streamer or flake in this side. The gap is closed and the stagnation region is not defined. (c) Perijove 21 (21 July 2019). This image was taken after the intense flake period in May-June 2019 and shows a ring of reddish material fully surrounding the red oval, probably due to the dispersion of the red chromophores from previous streamers and flakes (compare with (a) where the collar is well defined by the white clouds). The gap is not well defined and apparently appears to be closed since the stagnation region is also not evident.*

3.2 Effects on the dynamics of the GRS

The centre of the red oval moved throughout 2019 with a mean drift in longitude of 0.33 deg/day in System III, equivalent to a zonal velocity u = -4.5 ± 0.2 ms^{-1}, with no drifts in latitude (Figure S1). Coupled to it, the well known regular 90-day oscillation in longitude (Solberg, 1969; Trigo-Rodriguez et al., 2000) persisted, but was perturbed increasing the oscillation to 125 days around days 620-640 (mid-May to early June 2019) and the amplitude *A* from 1° to 1.2°, although the oscillation showed no phase shift in the longer term (Figures 7a, S2). The AV interactions forced the GRS natural oscillation preserving its maximum velocity $v_{\max} = A\omega \sim 0.9$ ms^{-1} (*A* from 1° to 1.2°, frequency $\omega = 2\pi/\tau$ and τ the oscillation period, from 90 to 125 days during intense interactions). The shape and size of the red oval underwent noticeable changes during interactions (Figure 7b). The east-west length decreased from 15.5° (18,040 km) in early March 2019 to 13.7° (15,950 km) in May 2020. Large fluctuations occurred during the period of intense flake formation with the zonal length reaching a minimum value of 13° (15,130 km). Figure 7c shows the area changes of the red oval considering it as an ellipse with the strongest decrease in area of 25%.

We tracked the motions of well-contrasted dark features internal to the red oval (Figures 1, 6) during intervals of ~ 1-3 days in ground-based images in 2019 April-June and April 2020 to determine their velocities. Only the best measured 45 vectors were considered for which we estimate a 10% error in their velocity (Figure 7d). Among them there are 22 vectors in the red oval periphery that give a mean velocity 149 ± 18 ms^{-1}, above the peak values of 120 ms^{-1} found on 17 April 2018 (Figure 1a) and in previous measurements (Simon et al., 2018; Sánchez-Lavega et al., 2018). Thus, the rotational velocity of the GRS accelerated following the AV interactions. However, the GRS maximum vorticity did not change. In 2018 it was ζ_V = 6.5x10^{-5} s^{-1} (Figure 2) and in 2019 we obtain to be ζ_V = 6.3x10^{-5} ± 1.2x10^{-5} s^{-1} using $\zeta_V \approx V_T\left[\frac{1}{b}\left(2-\frac{e^2}{2}\right)\right]$ (Legarreta and Sánchez-Lavega, 2005) that assumes an elliptical shape for the GRS (*a* = 5700 km and *b* = 4150 km are the semi-major and semi-minor axis of the ellipse), $e = \sqrt{1-\left(\frac{b}{a}\right)^2}$ is its eccentricity, and V_T = 150 ms^{-1} (data taken from Figure 7). These results are consistent with reported maximum velocities of 150 ms^{-1} and vorticity data from HST measurements in April and June 2019 (Wong et al., 2019).

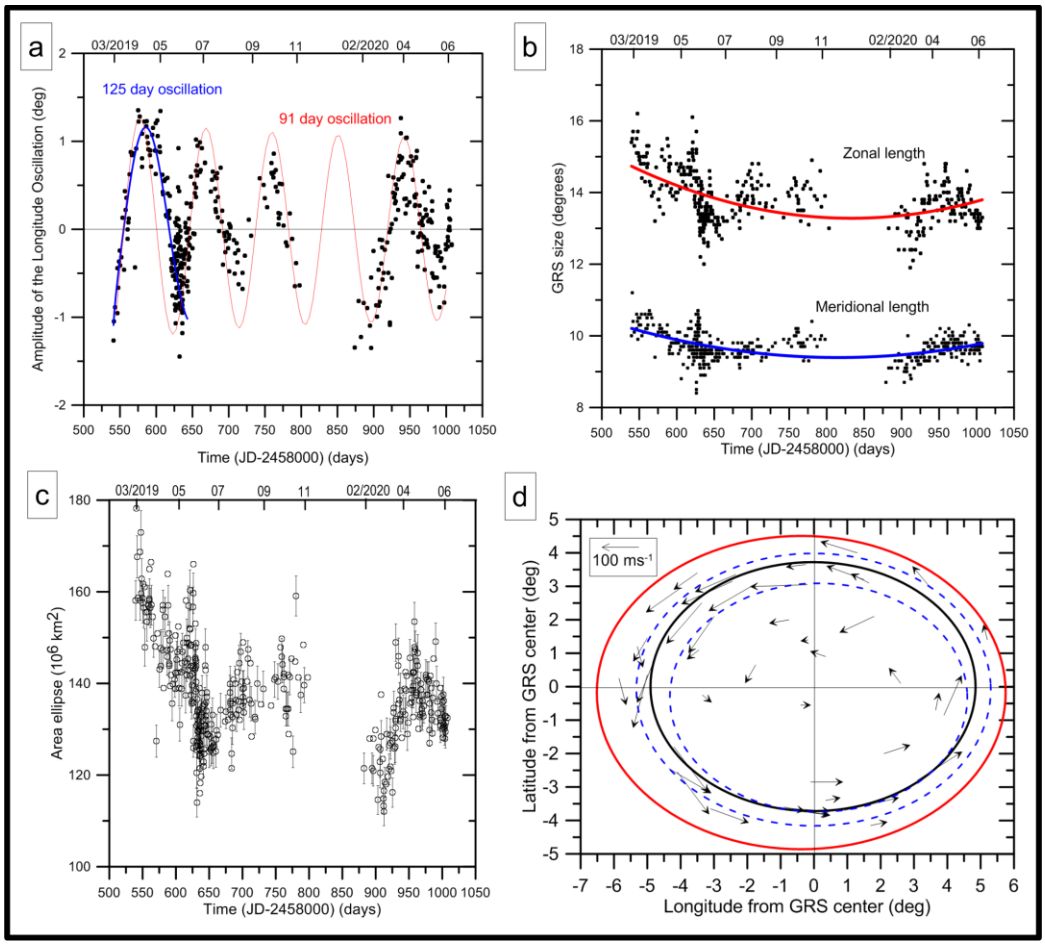

Figure 7. *Effects of the interactions on the GRS dynamics. (a) Oscillations in longitude of the centre of the GRS relative to its mean drift (Figure S1) and fits to a sinusoidal function with different periods and amplitudes. Bottom x-axis shows time Julian Date, while the corresponding month and year indicated at the top. (b) Zonal length (major axis) and meridional width (minor axis) of the GRS red oval area during the observing period. Typical errors in the size measurements range from ± 0.5° to ±1° depending on image quality. The red and blue curves show second-degree polynomial fits. (c) Area of the red ellipse from measurements in (b). Large fluctuations are seen in May-July 2019 (JD ~2458600 – 2458700) with strongest area decrease between JD ~2458550 – 2458625 (7 March to 21 May 2019). (d) Wind vectors from tracking the motions of distinct features in the GRS interior. Typical errors in the velocity measurements are ~10 ms^{-1}. The black line shows the ellipse where velocity has a maximum with uncertainty drawn by the internal and external ellipses drawn in dashed blue lines. The red line represents the edge of the red oval at the epoch of strongest interactions.*

3.3 Hazes and cloud models

We generated crude spectra in the wavelength range from 0.38 μm to 1.7 μm of the red oval and of a flake using images obtained in 27 May 2019 with PlanetCam astronomical camera (Mendikoa et al., 2016, 2017) (Figures 8, S3). The major differences between the GRS and the flake spectrum

occur at short wavelengths where the reflectivity *(I/F)* of the flake is always higher than that of the GRS. This spectral region is mainly sensitive to the particle number density and optical depth of the aerosol layers of the hazes. The description of the atmospheric parameters defining the aerosol vertical distribution in our radiative transfer model (see section 2.4) can be summarized as follows (Pérez-Hoyos et al., 2020): an uppermost stratospheric haze composed of small particles; an intermediate tropospheric haze of micron-sized particles which dominate the reflectivity measured in this work; and a bottom cloud with a limited effect on the modeling (Figure 8b, Table S3). While the uppermost and bottom aerosol layers were modeled with a single free parameter that accounts for the total optical thickness of the layer, the intermediate and most influential layer requires three free parameters for the vertical distribution (bottom pressure P_{bot}, peak particle density N and fractional scale height), two parameters to describe the particle size distribution (effective radius r_{eff} and dispersion σ) and the imaginary refractive index mi as a function of wavelength. The real refractive index was fixed to 1.43 at 890 nm and computed from the fitted imaginary values using the Kramers-Krönig relation as in (Lucarini et al., 2005). Previous works have shown that this kind of model accounts well for the observed reflectivity at this spectral resolution in both Jupiter (Pérez-Hoyos et al., 2020) and Saturn (Sánchez-Lavega et al., 2020a, 2020b).

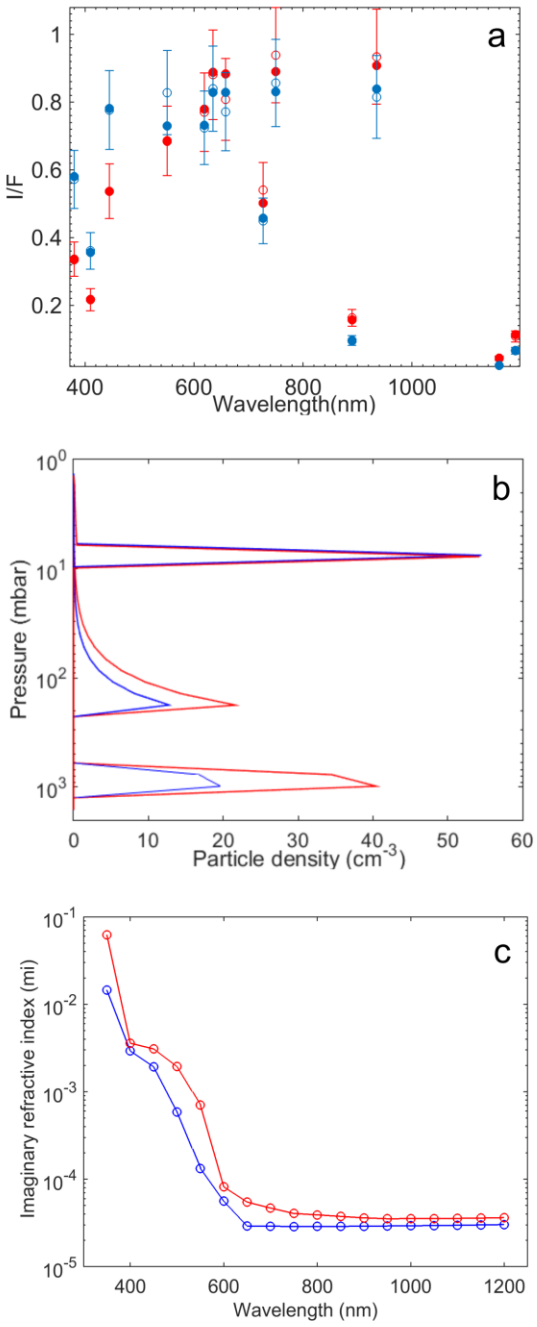

Figure 8. *Photometry and radiative transfer model of aerosol vertical distribution. (a) Absolute reflectivity (I/F) spectra of the centre of the GRS red core (red dots) and of a flake area (blue dots) obtained in 27 May 2019. The red and blue circles are the best model fits to the data; (b) The particle density as a function of altitude in the flake area (blue) and in the GRS (red) according to a radiative transfer model; (c) Refractive imaginary index of the tropospheric haze particles in the flake area (blue) and GRS (red) from the model (details given in Table S3).*

The model that best fits the spectra (Figure 8, Table S3) consists of a thin upper stratospheric haze layer located at P ~ 10 mbar with similar properties in the GRS and flake. Below it, there is a tropospheric haze with base at P ~ 200 mbar and a deeper cloud deck with base at P ~ 1 bar, consistent with previous studies (de Pater et al., 2010). It is in these two aerosol layers where we find the differences between the GRS and the flake. The particle density and the optical depth in the tropospheric haze and upper cloud deck are about 50% lower in the flake area than in the GRS core. The GRS is brighter than the flake in the red spectral region (including the methane absorption bands) because of the higher particle density, but the altitude of these two layers is similar. On the other hand, the flake is brighter in the violet-blue spectral region than the GRS because of the lower absorption by the haze particles (lower imaginary refractive index, Figure 8c). The simplest explanation for this difference is that the flake haze and cloud have lower particle density than the red oval, being material that has been plucked and separated from it, probably containing some mixture of particles from the AV. The cloud morphology shown in JunoCam colour images of the material outside the red oval supports this interpretation (Figures 1a, 3, 6a-b). The thin layer of red aerosols spread and overcast the clouds below it. The optical depth of the flake is low enough to allow seeing the deeper clouds below it suggesting that the flakes are "a surface phenomenon" that essentially affects the aerosol particle density above the 1-2 bar pressure level.

4 Dynamical interpretation

4.1 Numerical simulations of the dynamics of the interaction

We have used a shallow water model SW (García-Melendo and Sánchez-Lavega, 2017) and the EPIC multi-layer model (Dowling et al., 1998) to simulate the dynamics of the interaction between the GRS and an AV. The SW model is fast, retains a good deal of the large scale atmospheric physics and is justified for interactions between vortices with horizontal size >> vertical extent (Sánchez-Lavega et al., 2020a). The EPIC model allows to incorporate the vertical structure of the atmosphere and the altitude and vertical extent of the interacting vortices. The dynamic field is represented in both models by the Potential Vorticity, which acts as a material tracer of the flow. $\mathrm{PV} = \frac{f + \varsigma_V}{h}$ for the SW model and $\mathrm{PV} = \frac{(f + \varsigma_V)}{\rho}\left(\frac{\partial \theta}{\partial z}\right)$ for the EPIC model, where *h* is the layer thickness, ρ is the density, θ is the potential temperature, *z* the vertical coordinate, and $f = 2\Omega \sin\varphi$ the Coriolis parameter (Ω is Jupiter's angular velocity, φ the latitude) (Sánchez-Lavega, 2011). In both models we introduce two vortices, with horizontal size and velocity at periphery in the range of those of the GRS and AV respectively, into Jupiter's background wind velocity profile at their corresponding latitudes (Table S4).

The SW model uses Jupiter's zonal wind profile (Figure S4) that is continuously forced. A parallel version of the model (Sánchez-Lavega et al., 2020a) was run at the supercomputer Mare Nostrum 4 supercomputer (Barcelona, Spain) with a resolution of 0.05 per grid point and time step of 1 second, which was well below a 75% of the Courant–Friedrichs–Levy condition. Since the numerical integration is performed with fully explicit schemes, the parallelization with a domain-

decomposition strategy is very efficient. The GRS and AV the where introduced as a perturbation in geostrophic equilibrium. The model uses periodic conditions in longitude and full-slip (reflective) in latitude with no topography present. The Rossby radius of deformation of our model is $L_R = (gH)^{1/2}/f$ ~ 1200 km (gravity g = 25 ms^{-2}, SW layer depth H = 1000 m, Coriolis parameter f = 1.31x10^{-4} s^{-1}. The range of values of the parameters used in the simulations are given in Table S4A.

In Figure 9a we show the result of the SW simulations for the case of a strong interaction when AV has a tangential velocity at periphery V_T = 100 ms^{-1}. In such a case the AV impinges on the GRS southern flank, and as a consequence it stretches and lengthens, distorting the GRS oval shape and generating a large flake at its western side from material detached from the red oval. This case simulates very well the formation of the flakes (compare the western features with Figures 4-6). For weaker interactions when AV has V_T ~ 50 - 60 ms^{-1}, streamers and flakes also form but they are less prominent and the AV material does not penetrate the GRS. Penetration of the AV into the GRS and the formation of flakes instead of streamers, occur preferably when $V_T \geq$ ~ 100 ms^{-1} (Figure S5).

The EPIC model allows simulating interactions for different vertical extensions of the GRS and AV. The penetration depth of the PV anomaly for an axisymmetric vortex in hydrostatic and gradient-wind balance, like the GRS (Sánchez-Lavega et al., 2018), is given by (Wang et al., 1996)

$$D = \frac{L}{N}\left[\left(f + \varsigma_V\right)\left(f + \varsigma_{amb}\right)\right]^{1/2} \qquad (1)$$

Taking a Brunt-Väisälä frequency in the range N ~ 1 to 5x10^{-3} s^{-1} (de Pater et al., 2010), ambient vorticity (meridional shear of the zonal wind) $\varsigma_{amb} \approx \partial u / \partial y$ = 1.16x10^{-5} s^{-1} and horizontal scale of the flow L ~ 9000 km (peak to peak meridional distance in the zonal wind maxima north and south of the GRS) (Figure 1), f = -1.25x10^{-4} s^{-1} and GRS vorticity ζ_V = 6.5x10^{-5} s^{-1}, we get D_{GRS} ~ 290 - 1450 km. This range of values is consistent with the retrievals of the GRS depth derived from spectra obtained with Juno's infrared MWR experiment (Li et al., 2017) and from the study of the gravity field anomalies (Galanti et al., 2019a, 2019b) that indicate that the GRS extends at least down to the 240 bars deep level (or about 350 km below the ammonia upper cloud at 1 bar). We tested different vertical extents for the GRS (D_{GRS} ~ 200 - 300 km) centered at 0.68 bar level. We then apply a simple scale ratio between the horizontal size and depth for the vortices to take D_{AV} ~ 0.1-0.3 D_{GRS} in agreement with previous studies (de Pater et al., 2010).

For the EPIC simulations we define the structure of the atmosphere as shown in Figure S4 for a variety of situations and with the model parameters for Jupiter as defined in Morales-Juberías et al. (2003) and García-Melendo et al. (2009) with the tested range of values given in Table S4B. For the small anticyclones AV we have not measurements of the velocity at the periphery (rotation speed) and we estimate the range of values to use in the simulations assuming the vortex is in geostrophic balance with Rossby number in the range $Ro \sim V_T/fL$ ~ 0.07 - 0.15 that

445 follows our previous observations and models of Jovian anticyclones (Legarreta and Sánchez-
446 Lavega, 2005). Here *L* is the vortex size and *f* the Coriolis parameter that leads to tangential
447 velocities $V_T(AV)_{max}$ = 50-120 ms^{-1}.
448
449 In Figure 9b we show results from the EPIC simulations for an intermediate case in which the GRS
450 has twice the speed at its periphery than the AV and its vertical extent is three times that of it.
451 This case shows that as the interaction of the AV with the northern edge of the GRS progresses,
452 the AV vortex lengthens while penetrating the GRS, strongly distorting its shape. The stretched
453 AV becomes fragmented being dragged by the circulation of the GRS where it generates a wave
454 disturbance at the periphery of the red oval (Figure S6). This disturbance circulates through the
455 external part of the GRS while the elongated AV along with part of the red oval material separates
456 on its west side from it. Both the SW and EPIC model simulations form streamers and flakes and
457 strongly indicate that it is a "surface" phenomenon mainly occurring in the upper cloud layers of
458 the GRS.
459

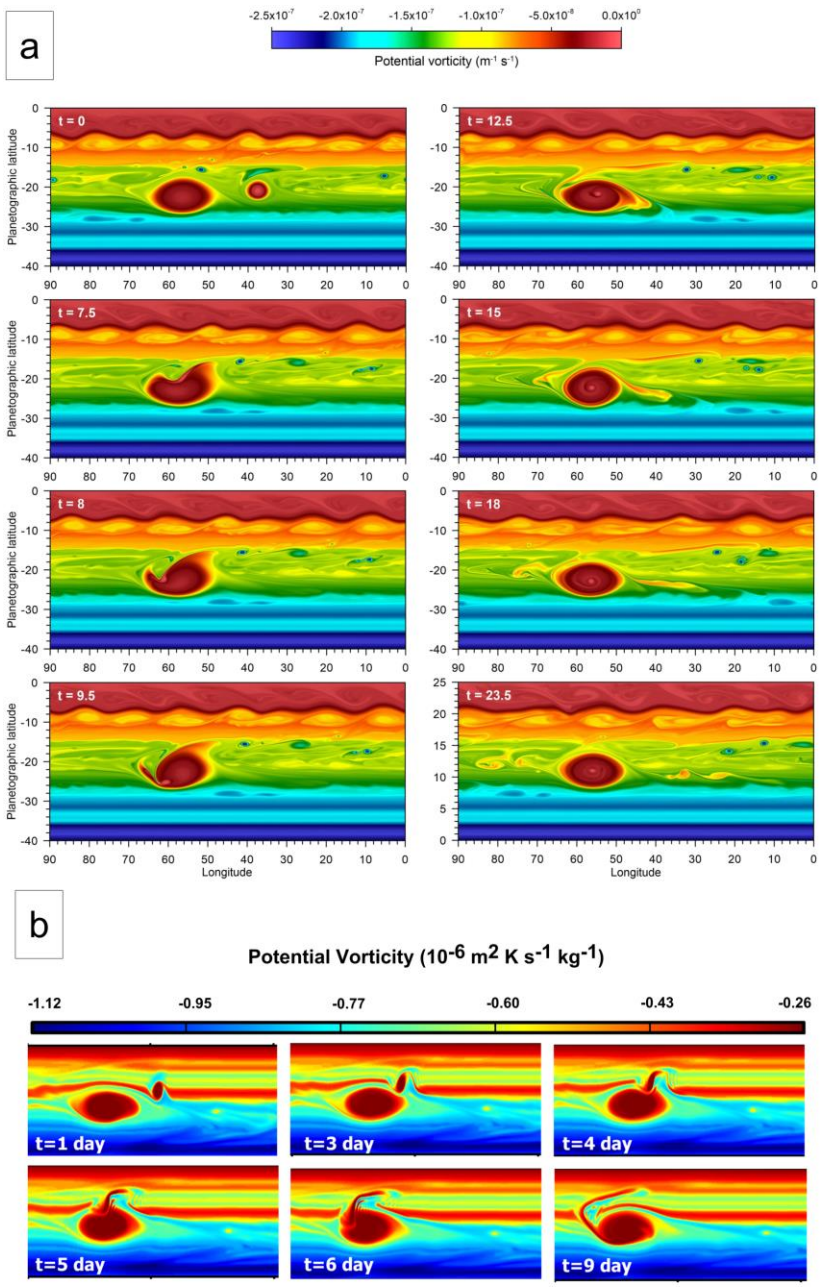

Figure 9. *Numerical simulations of the interactions of the GRS and an AV anticyclone. Potential Vorticity maps for two type of models: (a) SW simulations of the interaction for the GRS with peak tangential velocity V_T = 100 m/s and for AV at latitude 20.0°S. Time (t) is given in days. (b) EPIC simulations with V_T = 100 ms^{-1} (GRS) and V_T = 50 ms^{-1} (AV), with a vertical extent of 6 scale heights (~120 km) for GRS and 2 scale heights (~40 km) for AV, with both vortices centered at pressure level P = 680 mbar. Other data are given in Table S4.*

4.2 GRS dynamics

An AV that is totally absorbed by the GRS adds energy (per unit mass) due to its own rotation, $E_{rot} \approx (1/2)V_{rot}^2 \sim$ 1250 J kg^{-1}, and its velocity, $E_k \approx (1/2)u^2 \sim$ 800 J kg^{-1} (V_T = 100 ms^{-1}, u = 40 ms^{-1} relative to GRS) (Figure 4). If this energy is totally converted into heat during the frictional and mixing processes, the temperature must increase in the outer part of the GRS where the vortex is absorbed by $\Delta T \approx \left(E_{rot} + E_k\right)/C_p \sim$ 0.2 K, where C_p = 12360 JKg^{-1}K^{-1} , the specific heat at constant pressure. This is an upper value since the energy losses, e.g. radiative, have not been considered. The added energy will increase the radial temperature gradient $(dT/dr)_P$ in the GRS interior and assuming the vortex is under gradient wind balance (Mitchell et al., 1981; Sánchez-Lavega et al., 2018), we can estimate the change in its rotational velocity from the use of the thermal wind balance (Flasar et al., 1981; Pérez-Hoyos et al., 2009; Fletcher et al., 2010),

$$\frac{\partial \mathrm{V}_T}{\partial \ln P} = -\frac{R_g^*}{(f+\varsigma_V)}\left(\frac{\partial T}{\partial r}\right)_P \qquad (2)$$

We take the wind measurements at a pressure level P = 600 mbar and we assume null speed at 20 mbar (Conrath et al., 1981) both before and after the interactions. The altitude difference between these two levels is $\ln(600/20) = 3.4$ scale heights and take $(f+\zeta_V) \sim$-6.5x10^{-5} s^{-1} (in 2018 and 2019), R_g^* = 3750 JKg^{-1}K^{-1}. From (2) we get an average horizontal temperature gradient of $\left(\partial T/\partial r\right)_P =$-6x10^{-4} K km^{-1} in 2018 and -7.75x10^{-4} K km^{-1} in 2019. We then calculate temperature difference between the GRS centre and the collar with peak vorticity (average distance r) using that gradient at the semi-major axis and semi-minor axis of the ellipse that defines the collar of maximum vorticity (a = 4420 km, b = 2805 km in 2018 from Figure 2; a = 5700 km, b = 4150 km in 2019 from Figure 7). This gives $\Delta T \approx -\left(\frac{\partial T}{\partial r}\right)_P r \sim$ 2.2 K (ΔT = 2.6 K and 1.7 K at a and b) to have V_T *(max)* = 120 ms^{-1} (in 2018), and $\Delta T \sim$ 3.8 K (ΔT = 4.4 K and 3.2 K at a and b) to have V_T *(max)* = 150 ms^{-1} (in 2019). These rough numbers agree with previously measured temperature contrasts in the GRS (Fletcher et al., 2010).The deposited energy from AVs is multiplicative with the number of vortices interacting with the GRS, which was only 0.17 per month averaged from 2016 March to 2018 June, but 2.0 per month averaged from 2019 March to June. Thus, a moderate heating due to energy absorption provided by the AVs as calculated above could produce the observed increase in the peak tangential velocity at cloud tops.

5 Conclusions

In 2018-2020, Jupiter's Great Red Spot long lifetime survival appeared to be threatened following strong interactions with series of smaller anticyclonic vortices (AV), giving rise to the following events:

- The GRS increased its maximum tangential velocity up to 150 ms^{-1}.

- The GRS vorticity do not changed.
- The visible red area decreased when the AVs tore off large fragments and distorted its shape.
- The GRS suffered a transient change in its steady 90-day oscillation in longitude, increasing its period and amplitude.

From a radiative transfer analysis of the GRS reflectivity in the visual and near infrared wavelengths we have shown that the interactions affected the upper cloud tops of the GRS. This is also confirmed by numerical simulations of the dynamics of these interactions using a shallow water model and a general circulation model.

Encounters between anticyclones of similar size lead to complete mergers (Mac Low and Ingersoll, 1986), as was the case of the large and long-lived three White Ovals that generated twenty years ago a single steady anticyclone BA (length ~ 11,000 km, about half the GRS current size) (Sánchez-Lavega et al., 1999, 2001) with a similar velocity field to its predecessors and to the GRS (Hueso et al., 2009). However, the GRS interactions behave differently since it is a single anticyclone at its latitude. The GRS has been slowly decreasing in size since the late nineteenth century (Rogers, 1995; Simon et al., 2018), and in 2019 the interactions with AVs reduced the visible red oval to the smallest size ever recorded while increasing peak velocities but preserving its vorticity (within the precision of ground-based measurements). The flaking events are likely to have been superficial, not affecting the full depth of the GRS. Indeed, by October 2019, the visible red oval had almost recovered to its previous size (Figure 7). Our analysis shows that the ingestion of AVs is not necessarily destructive (Vasavada and Showman, 2005); it can increase the GRS wind speed, and perhaps over a longer period, maintain it in a steady state (Dowling et al., 1989; Sada et al., 1996). The intense vorticity of the GRS, together with its larger size and depth, compared to the interacting vortices, guarantees its long lifetime.

References

Acton C. H. (2016). Ancillary data services of NASA's Navigation and Ancillary Information Facility, *Planetary and Space Science*, *44*, 65-70.

Caplinger M. (2016). Malin Space Science Systems Inc., in Juno, Software Interface Specification, JunoCam Standard Data Products Version 1.3. Available at NASA PDS: https://pds-imaging.jpl.nasa.gov/data/juno/JNOJNC_0001/DOCUMENT/JUNO_JNC_EDR_RDR_DPSIS.PDF

Conrath B. J., Flasar F. M. & Pirraglia J. A. (1981). Thermal Structure and Dynamics of the Jovian Atmosphere 2. Visible Cloud Features, *J. Geophys. Res.*, *86*, 8769-8775.

de Pater I., Wong M. H., Marcus. P., Luszcz-Cook S., Ádámkovics M., Conrad A., Asay-Davis X. & Go C. (2010). Persistent rings in and around Jupiter's anticyclones – Observations and theory, *Icarus*, *210 (2)*, 742-762.

552 Dowling, T.E., Fisher, A.S., Gierasch, P.J., Harrington, J., LeBeau, R.P. & Santori, C.M. (1998). The
553 explicit planetary isentropic-coordinate (EPIC) atmospheric model, *Icarus*, *132*, 221–238.
554
555 Dowling T. E. & Ingersoll A. P. (1989). Jupiter's Great Red Spot as a Shallow Water System, *J.*
556 *Atmos. Sci.*, *46*, 3256-3278.
557
558 Flasar F. M., Conrath B. J., J. A. Pirraglia, P. C. Clark, R. G. French & Gierasch P. J. (1981). Thermal
559 Structure and Dynamics of the Jovian Atmosphere 1. The Great Red Spot, *J. Geophys. Res*., *86*,
560 8759-8767.
561
562 Fletcher L. N., Orton G.S., Mousis O., Yanamandra-Fisher P. et al. (2010). Thermal structure and
563 composition of Jupiter's Great Red Spot from high-resolution thermal imaging, *Icarus*, *208*, 306-
564 328.
565
566 Foster C., Rogers J. H., Mizumoto S., Casely A. & Vedovato M. (2020). Jupiter in 2019 Report
567 no.10: The GRS in 2019 and its interaction with retrograding vortices as monitored by the
568 amateur planetary imaging community, https://britastro.org/node/22552.
569
570 Galanti, E., Kaspi, Y., Simons, F.J., Durante, D., Parisi, M. & Bolton, S.J. (2019a). Determining the
571 depth of Jupiter's Great Red Spot with Juno: a slepian approach. *Astrophys. J. Lett.* 874: L24 (7pp)
572 https://doi.org/10.3847/2041-8213/ab1086.
573
574 Galanti, E., Kaspi Y., Parisi M., Folkner W. M., Durante D., Simons, F.J. & Bolton, S.J. (2019b). How
575 deep is the Great Red Spot? A multimethod analysis using the recent Juno gravity.
576 Measurements, EPSC-DPS Joint Meeting, *EPSC Abstracts*, Vol. 13, EPSC-DPS2019-1228-1.
577
578 García-Melendo, E., Legarreta, J., Sánchez-Lavega, A., Hueso, R., Pérez-Hoyos, S., González, J.,
579 Gómez-Forrellad, J.M. & IOPW Team (2009), The jovian anticyclone BA: I. Motions and interaction
580 with the GRS from observations and non-linear simulations, *Icarus*, *203*, 486-498.
581
582 García-Melendo E. & Sánchez-Lavega A. (2017). Shallow Water simulations of Saturn's Giant
583 Storms at different latitudes, *Icarus, 286*, 241-260.
584
585 GDAL/OGR contributors (2020). GDAL/OGR Geospatial Data Abstraction software Library. Open
586 Source Geospatial Foundation. URL https://gdal.org
587
588 Hueso R., Legarreta J., García-Melendo E., Sánchez-Lavega A. & Pérez-Hoyos S. (2009). The Jovian
589 anticyclone BA: II. Circulation and models of its interaction with the zonal jets, *Icarus*, *203*, 499-
590 515.
591
592 Irwin, P. G. J., Teanby, N. A., de Kok, R., Fletcher, L. N., Howett, C. J. A., Tsang, C. F. Wilson, S. B.
593 Calcutt, C. A. Nixon & Parrish, P. D. (2008). The NEMESIS planetary atmosphere radiative transfer
594 and retrieval tool. *J. of Quant. Spec. and Radiative Transfer*, *109* , 1136-1150. doi:
595 10.1016/j.jqsrt.2007.11.006

Karkoschka, E., & Tomasko, M. G. (2010). Methane absorption coefficients for the Jovian planets from laboratory, Huygens, and HST data, *Icarus*, *205*, 674-694. doi: 10.1016/j.icarus.2009.07.044.

Legarreta J. & Sánchez-Lavega A. (2005). Jupiter's Cyclones and Anticyclones Vorticity from Voyager and Galileo Images, *Icarus, 174*, 178-191.

Li, L., Ingersoll, A.P., Vasavada, A.R., Porco, C.C., Del Genio, A.D. & Ewald, S.P. (2004). Life cycles of spots on Jupiter from Cassini images*, Icarus, 172*(1), 9-23.

Li, C., Oyafuso, F.A., Brown, S.T., Atreya, S.K., Orton, G.S., Ingersoll, A.P. & Janssen, M.A. (2017). How Deep Is Jupiter's Great Red Spot? Paper Presented at American Geophysical Union Fall Meeting 2017, American Geophysical Union, New Orleans (Louisiana, USA). http://refhub.elsevier.com/S0032-0633(19)30059-5/sref23

Lucarini, V., Saarinen, J.J., Peiponen, K.E. & Vartiainen, E.M. (2005). Kramers–Kronig Relations in Optical Materials Research, Springer-Verlag Berlin Heidelberg, Germany.

Mac Low M. & Ingersoll A. P. (1986). Merging of vortices in the atmosphere of Jupiter: An analysis of Voyager images, *Icarus*, *65*, 353-369.

Mendikoa I., Sánchez-Lavega A., Pérez-Hoyos S., Hueso R., Rojas J. F., Aceituno J., Aceituno F. J., Murga G., de Bilbao L. & García-Melendo E. (2016). PlanetCam UPV/EHU: A two channel lucky imaging camera for Solar System studies in the spectral range 0.38-1.7 μm, *Pub. Astron. Soc. Pacific*, *128*, 035002 (22 pp).

Mendikoa I., Sánchez-Lavega A., Pérez-Hoyos S., Hueso R., Rojas J. F. & López-Santiago J. (2017). Temporal and spatial variations of Jupiter's and Saturn's absolute reflectivity from 0.38 to 1.7 μm using PlanetCam-UPV/EHU, *Astronomy & Astrophys.*, *607*, A72 doi: 10.1051/0004-6361/201731109.

Mitchell J. L., Beebe R. F., Ingersoll A. P. & Garneau G. W. (1981). Flow Fields within Jupiter's Great Red Spot and White Oval BC, *J. Geophys. Res*., *86*, 8751-8757.

Morales-Juberías R., Sánchez-Lavega A. & Dowling T. (2003). EPIC simulations of the merger of Jupiter's White Ovals BE and FA: Altitude dependent behavior, *Icarus, 166*, 63-74.

Pérez-Hoyos S., Sánchez-Lavega A., Hueso R., García-Melendo E. & Legarreta J. (2009). The Jovian anticyclone BA: III. Aerosol properties and colour change, *Icarus, 203*, 516-530.

Pérez-Hoyos S., Sánchez-Lavega A., Sanz-Requena J.F., Barrado-Izagirre N., Carrión-González O., Anguiano-Arteaga A., Irwin P.G.J. & Braude A. S. (2020). Color and aerosol changes in Jupiter after a North Temperate Belt disturbance, *Icarus, 132*, 114021.

Rogers, J. H. (1995). The Giant Planet Jupiter, p. 188-197, Cambridge Univ. Press, Cambridge, U. K.

Rogers J. H., Eichstädt G., Jacquesson M., Hansen C.J., Orton G. S., et al. (2018). The new South Tropical Disturbance and its interaction with the Great Red Spot, *EPSC Abstracts*, Vol. 12, EPSC2018-562, European Planetary Science Congress.

Sada, P. V., Beebe R. F. & Conrath B. J. (1996). Comparison of the Structure and Dynamics of Jupiter's Great Red Spot between the Voyager 1 and 2 Encounters, *Icarus, 119*, 311-335 (1996).

Sánchez-Lavega, A., Hueso, R., Lecacheux, J., Colas, F., Rojas, J.F., Gomez, J.M., Miyazaki & I., Parker, D. (1998). Dynamics and interaction between a large-scale vortex and the Great Red Spot in Jupiter, *Icarus 136*, 14–26.

Sánchez-Lavega, A., Rojas, J.F., Hueso, R., Lecacheux, J., Colas, F., Acarreta, J.R., Miyazaki, I. & Parker, D. (1999). Interaction of Jovian White Ovals BC and DE in 1998 from Earth-based observations in the visual range, *Icarus 142*, 116–124.

Sánchez-Lavega, Orton G.S., Morales R., Lecacheux J., Colas F., Fisher B. et al. (2001). The merger of two giant anticyclones in the atmosphere of Jupiter, *Icarus 149*, 491–495.

Sánchez-Lavega A. (2011), An Introduction to Planetary Atmospheres, Taylor-Francis, CRC Press, Florida, pp. 629

Sánchez-Lavega A., Legarreta J., García-Melendo E., Hueso R., Pérez-Hoyos S. et al. (2013). Colors of Jupiter's large anticyclones and the interaction of a Tropical Red Oval with the Great Red Spot in 2008, *J. Geophys. Res.***,** *118*, 1-21**.**

Sánchez-Lavega A., Hueso R., Eichstädt G., Orton G., Rogers J., Hansen C. J., Momary T., Tabataba-Vakili F. & Bolton S. (2018). The rich dynamics of Jupiter's Great Red Spot from JunoCam – Juno images, *Astronomical J.*, 156, 162 (9pp).

Sánchez-Lavega A., García- Melendo E., Legarreta J., Hueso R., del Río-Gaztelurrutia T., et al. (2020a). A complex storm system and a planetary-scale disturbance in Saturn's north polar atmosphere in 2018, *Nature Astronomy, 4*, 180-187, https://doi.org/10.1038/s41550-019-0914-9

Sánchez-Lavega A., Garcia-Munoz A., del Rio-Gaztelurrutia T., Perez-Hoyos S., Sanz-Requena J. F., Hueso R., Guerlet S. & Peralta J. (2020b). Multilayer hazes over Saturn's hexagon from Cassini ISS limb images, *Nature Communications*, 11, 2281.

Simon A. A., Tabataba-Vakili F., Cosentino R., Beebe R. F., Wong M. H., & Orton G. S. (2018), Historical and Contemporary Trends in the Size, Drift, and Color of Jupiter's Great Red Spot, *Astronomical. J.*, 155:151 (13pp).

Smith B. A. et al. (1979). The Jupiter System Through the Eyes of Voyager 1, *Science, 204*, 951-972.

Solberg H.G. (1969), A 3-month oscillation in the longitude of Jupiter's Red Spot**,** *Planet. Space Sci.*, 17, 1573-1580.

Taylor, F. W., Atreya, S. K., Encrenaz, T., Hunten, D. M., Irwin, P. G. J., & Owen, T. C. (2004). The composition of the atmosphere of Jupiter, in F. Bagenal, T. E. Dowling & W. B. McKinnon (Eds.), Jupiter: The planet, satellites and magnetosphere, Vol. 1, p. 59-78.

Trigo-Rodríguez J. M., Sánchez-Lavega A., Gómez J. M., Lecacheux J., Colas F. & Miyazaki I. (2000). The 90-day oscillations of Jupiter's Great Red Spot revisited, *Plan. Space Sciences*, *48*, 331-339.

Vasavada A. R. & Showman A. P. (2005). Jovian atmospheric dynamics: an update after Galileo and Cassini, *Rep. Prog. Phys.*, *68*, 1935-1996.

Wang Y. & Holland G. (1996). The beta drift of baroclinic vortices. Part I: adiabatic vortices, *J. Atmos. Sci., 53*, 411- 427.

Wong M., de Pater I., Simon A. A. & Marcus P. S. (2019). Jupiter's Great Red Spot Is Not Disintegrating by Flaking Apart. Poster P13B-3502, American Geophysical Union Fall Meeting, San Francisco.

Wong M. H., Simon A. A., Tollefson J. W., de Pater I., Barnett M. N., et al. (2020). High-resolution UV/Optical/IR Imaging of Jupiter in 2016–2019, *Astrophys. J. Suppl. Ser., 247*: 58 (25pp) doi.org/10.3847/1538-4365/ab775f

WinJUPOS (accesed 2020). http://www.grischa-hahn.homepage.t-online.de/

Acknowledgments

This work has been supported by the Spanish project AYA2015-65041-P and PID2019-109467GB-I00 (MINECO/FEDER, UE) and Grupos Gobierno Vasco IT1366-19. PI acknowledges a PhD scholarship from Gobierno Vasco. EGM is Serra Hunter Fellow at UPC. This work has used data acquired from the NASA/ESA HST Space Telescope, which is operated by the Association of Universities for Research in Astronomy, Inc., under NASA contract NAS 5-26555. These HST observations are associated with program GO/DD 15262. PlanetCam observations were collected at the Centro Astronómico Hispánico en Andalucía (CAHA), operated jointly by the Instituto de Astrofisica de Andalucia (CSIC) and the Andalusian Universities (Junta de Andalucía). EGM, MS, APG, MAC and ASL thankfully acknowledge the computer resources at Mare Nostrum and the technical support provided by Barcelona Supercomputing Center (AECT-2019-2-0006). This research has made use of the USGS Integrated Software for Imagers and Spectrometers (ISIS). We appreciate the contribution from all observers cited in Table S1 for his fundamental

contribution to this study with Jupiter images obtained with high dedication and skill. GSO and TM were supported by NASA with funds distributed to the Jet Propulsion Laboratory, California Institute of Technology.

Data availability

The data that support the plots within this paper and other findings of this study are available from the corresponding author upon reasonable request. This work relies in images that can be downloaded from the following sources:
Association of Lunar and Planetary Observers ALPO – Japan:
http://alpo-j.sakura.ne.jp/Latest/Jupiter.htm
PVOL2 database: http://pvol2.ehu.eus/pvol2/
HST-OPAL program:
https://archive.stsci.edu/prepds/opal/
Juno/Junocam images at NASA PDS (Planetary Data System):
https://pds-imaging.jpl.nasa.gov/
PlanetCam images are available from the corresponding author.
The navigation software WinJupos is available at: http://jupos.org/gh/download.htm
The image correlation software PICV is available upon request from Ricardo Hueso (ricardo.hueso@ehu.eus).
The radiative transfer code NEMESIS (http://users.ox.ac.uk-/atmp0035/nemesis.html) is available upon request from Patrick Irwin (patrick.irwin@physics.ox.ac.uk)
The shallow water model code is available from Enrique García-Melendo (enrique.garcia.melendo@upc.edu) upon request.
The EPIC numerical model is an open-code funded by NASA, see details:
http://surveygizmoresponseuploads.s3.amazonaws.com/fileuploads/15647/4054745/254-fd0a70105de25e281834d7f5dcc5451c_DowlingTimothyE.pdf